Mechatronics 20 (2010) 686–697

Contents lists available at ScienceDirect

Mechatronics

journal homepage: www.elsevier.com/locate/mechatronics

Control of McKibben pneumatic muscles for a power-assist, lower-limb orthosis

T.-J. Yeh *, Meng-Je Wu, Ting-Jiang Lu, Feng-Kuang Wu, Chih-Ren Huang

Department of Power Mechanical Engineering, National Tsing Hua University, Hsinchu, Taiwan

ARTICLE INFO

Article history:
Received 7 October 2009
Accepted 15 July 2010

Keywords:
Pneumatic muscle
Lower-limb orthosis
Hysteresis
Maxwell-slip model
LTR control
Bumpless switching

ABSTRACT

In this research, a power-assist, lower-limb orthosis is developed to help the elderly or people suffering sports injuries walk or climb stairs. In the pneumatic muscle used for actuation, it is found that hysteresis phenomenon exists during the inflation–deflation process and such a phenomenon deteriorates the control performance. In order to eliminate the influence of hysteresis on the control system, a hysteresis model is constructed and used to devise an inverse control for feedforward compensation. The inverse control is combined with loop transfer recovery (LTR) feedback control to achieve better tracking performance. Moreover, bumpless switching compensators are also incorporated into the combined control system to ensure smooth switching between different phases of operation. To verify that the developed orthosis can effectively accomplish the assistive function, a human subject wearing the orthosis is asked to walk and to climb stairs. Experiments indicate that the orthosis is indeed helpful in assisting human locomotion.

1. Introduction

The pneumatic muscle actuator, or so-called McKibben pneumatic artificial muscle, was developed in the 1950s and 1960s for artificial limb research [1,2]. It consists of a rubber inner tube surrounded by a braided mesh shell. When the inner tube is pressurized, it expands in a balloon-like manner but the expansion is constrained by the braided shell. As the volume of the inner tube increases with the increase of pressure, the pneumatic muscle shortens and/or produces tension if it is coupled to a mechanical load.

The pneumatic muscles are well-known for their exceptionally high power and force to weight/volume ratios. Moreover, they are inherently compliant that can generate soft contact and thus have excellent safety potential. These attractive features make the pneumatic muscle a promising actuation source for robotic exoskeleton or powered orthoses applications where not only safety for human interaction is needed but also lightweight actuation design is desired. For instance, Kobayashi et al. [3] developed a muscle suit for supporting manual worker. The muscle suit consists of a mechanical armor-type frame and pneumatic muscles. Zhang et al. [4] proposed a novel curved pneumatic-muscle-based rotary actuator for a wearable elbow exoskeleton. A powered ankle–foot orthosis (AFO) that uses artificial pneumatic muscles was developed by Ferris et al. to produce active plantar flexor torque [5]. Extension of AFO to a knee–ankle–foot orthosis (KAFO), which uses pneumatic muscles to power ankle plantar flexion/dorsiflexion as well as knee extension/flexion, has also been considered in [6]. In [7], a 10 DOF lower limb exoskeleton with legs powered by pneumatic muscles was constructed for force augmentation and active assistive walking training.

It should be noted that the above-mentioned references mainly focus on the overall system design and performance evaluation. Sophisticated behavior of pneumatic muscles are not particularly incorporated into the controller design. Instead, the forces or torques generated by pneumatic muscles therein are simply achieved either by regulating the air pressures to fixed settings [3] or according to the processed electromyography (EMG) [5,6], via simple PID controllers [7], or black-box based fuzzy controllers [4]. In order to better understand the behavior of pneumatic muscles for not only control but also design purposes, several research efforts have been devoted to the modeling of such actuators. For instance, the model in [8] shows that pneumatic muscles exhibit a nonlinear force–displacement relationship. Moreover, it is demonstrated in [9,10] that the thread-on-thread friction acting inside the braided shell further induces hysteretic behavior to such a nonlinear model. In [11], Klute and Hannaford developed a model that predicts the maximum number of life cycles of the pneumatic muscle actuator based on available uni-axial tensile properties of the actuator's inner bladder. In [12], the same authors presented another model that includes a nonlinear, Mooney–Rivlin mathematical description of the actuator's internal bladder. It is shown experimentally that the model provides more accurate prediction on the actuator's output force. In [13], a phenomenological model

* Corresponding author. Tel.: +886 35742922; fax: +886 35722840.
E-mail address: tyeh@pme.nthu.edu.tw (T.-J. Yeh).

0957-4158/$ - see front matter © 2010 Elsevier Ltd. All rights reserved.
doi:10.1016/j.mechatronics.2010.07.004

which characterizes the pneumatic muscle as a parallel combination of a contractile element, a pressure-dependent damping element, and a pressure-dependent spring element is proposed. Experiments indicate that the model can describe the dynamic response to the step pressure input accurately. Another interesting works were done in [14,15] in which biomechanical intelligence is incorporated into pneumatic muscles to make them behave more similar to the biological muscles. The authors therein placed a hydraulic damper in parallel with the pneumatic muscle. By doing so, the combined device can have not only muscle-like force–length properties, but also muscle-like force–velocity properties.

As revealed by the above modeling literature, the pneumatic muscles exhibit quite complex characteristics. Therefore, advanced control designs capable of dealing with these complex characteristics can certainly enhance the performance of pneumatic muscles. This is the reason why in the literature, control schemes including sliding-mode control [16,17], nonlinear PID using a neural network [18], flatness-based nonlinear control [19], and adaptive control [20] have been proposed for pneumatic muscles.

In this research, control of pneumatic muscles for a power-assist, lower-limb orthosis is considered. The orthosis is to generate appropriate assistive knee torque to help the elderly or people suffering sports injuries walk or climb stairs. During the inflation–deflation of the pneumatic muscle, it is experimentally observed that hysteresis phenomenon is substantial and such a phenomenon tends to deteriorate the control performance. Because the hysteresis phenomenon is seldom characterized in the associated modeling literature [8–15], in order to avoid control performance degradation, a modified maxwell-slip model is proposed to characterize hysteresis and is used to derive an inverse model for cancelling the hysteresis effect. Moreover, the nature of walking demands the orthosis to be operated in two phases: stance phase and swing phase. Smooth switching between the two phases is critical for not only user's comfort but also the effectiveness of the orthosis. Therefore, bumpless switching compensators are incorporated into the control system to ensure smooth switching between these two phases of operation. The paper is organized as follows: In Section 2, the design of the orthosis is described. Section 3 presents the modified maxwell-slip model and the associated inverse control method. The inverse control is integrated with the two LTR controllers introduced in Section 4 to achieve better performance respectively in tension tracking and angle tracking. In this same section, the bumpless switching compensation is also discussed. In Section 5, three types of experiments are conducted to examine the performance of the control system designed for the powered orthosis. Finally, conclusions are given in Section 6.

2. Orthosis design

2.1. Device description

The photo of the orthosis developed is shown in Fig. 1a. It basically consists of a pneumatic muscle, a zig-zag-shaped steel wire, an electronically-controller pressure valve, a pressure shoe, and relevant sensors. As shown in the mechanical schematic of Fig. 1b (in which the sensors and the valve are omitted), the tension-only pneumatic muscle is connected via pulleys to the zig-zag steel wires on both sides of the knee in a parallel manner. The steel wire in this case performs the function of a torsional spring to pre-stretch the pneumatic muscle. The zig-zag shape is especially designed so that under the tension of the pneumatic muscle, the deformation of steel wire is compatible with the rotation motion of the knee so that the two braces which fix the ends of the wire do not move relatively to the leg as the pneumatic muscle is actuated.[1] When receiving electronic signals, the pressure valve (ITV1031-312BL, SMC) modulates the pressure of the pneumatic muscle so as to produce the bidirectional assistive torque.

There are no other gearings attached to the knee and the ankle joint is allowed to rotate freely. There are seven load cells embedded in the sole of the pressure shoe.[2] The measurements from the load cells are used to compute the ground reaction force and the corresponding center of pressure (COP). A tension sensor (LC201–300, Omega) is placed in series with the pneumatic muscle to measure muscle tension. There are also two potentiometers respectively located at the knee and the ankle to measure the associated angles of rotation. When the orthosis is in operation, the user has to carry a backpack. Other than the pressure control valve mentioned, the backpack also contains a battery, compressed carbon-dioxide (CO_2) tanks as the pneumatic source, gas accumulators, and a digital-signal-processor (TMS320F2812eZdsp). The digital-signal-processor, equipped with 12-bit A/D and 12-bit D/A, implements the control system.

For decoration and protection purposes, there are plastic covers attached to the major components of the orthosis. The picture of a person wearing the overall system is shown in Fig. 2.

2.2. Control philosophy

In principle, the leg motion can be characterized into two phases: the stance phase and the swing phase. During the stance phase, either the whole or the partial body weight is supported by the leg. During the swing phase, the leg does not support the body weight but the joints are bent or unbent to generate the motion intended. For instance, during walking, each of the legs experiences the stance phase and the swing phase alternatively. During standing up, both legs are in the stance phase. The developed orthosis is controlled differently for the two phases. During the stance phase, tension control is performed on the pneumatic muscle to generate assistive knee torque so that the force required by the quadriceps muscle is reduced compared to what would be required without the orthosis. During the swing phase, trajectory control is performed on the pneumatic muscle so that the (knee) angle of the orthosis follows a pre-designed trajectory that is compatible with the leg's natural swing motion.

2.3. Determination of assistive knee torque

The merit of the orthosis developed mainly lies in the assistive knee torque it provides during the stance phase. The assistive knee torque is chosen as a fixed percentage of the knee torque needed to support the body weight. The knee torque for weight support, denoted by τ_w, is determined using the simplified shank–foot model in Fig. 3. Three assumptions are made to derive the knee torque. Firstly, assume that the motion is gentle and slow so that the dynamic effect can be ignored. Secondly, ignoring the dynamic effect means that the horizontal acceleration of the human operator is negligible, so the horizontal, frictional component of the ground reaction is ignored in Fig. 3. Finally, the weight of the shank is ignorable because it is small compared to the body weight. With

[1] The torsional spring constituted by the steel wire needs to follow a predefined loading–displacement relationship so that the braces holding the ends of the wire do no move relatively to the leg during the actuation of pneumatic muscle. To design the spring, the spring's shape was firstly assumed to be a cubic spline curve then a modified Castigliano's second theorem was used to determine the geometric parameters associated with the curve. The computational results showed that in order to achieve the predefined loading–displacement relationship, the steel wire needs to be bent into a zig-zag shape. For details on the design of the zig-zag steel wire, the readers can refer to [21].

[2] The load cells in the pressure shoe include one LM-100KA, and six LM-50K's, all of which are manufactured by Kyowa, Inc., Japan.

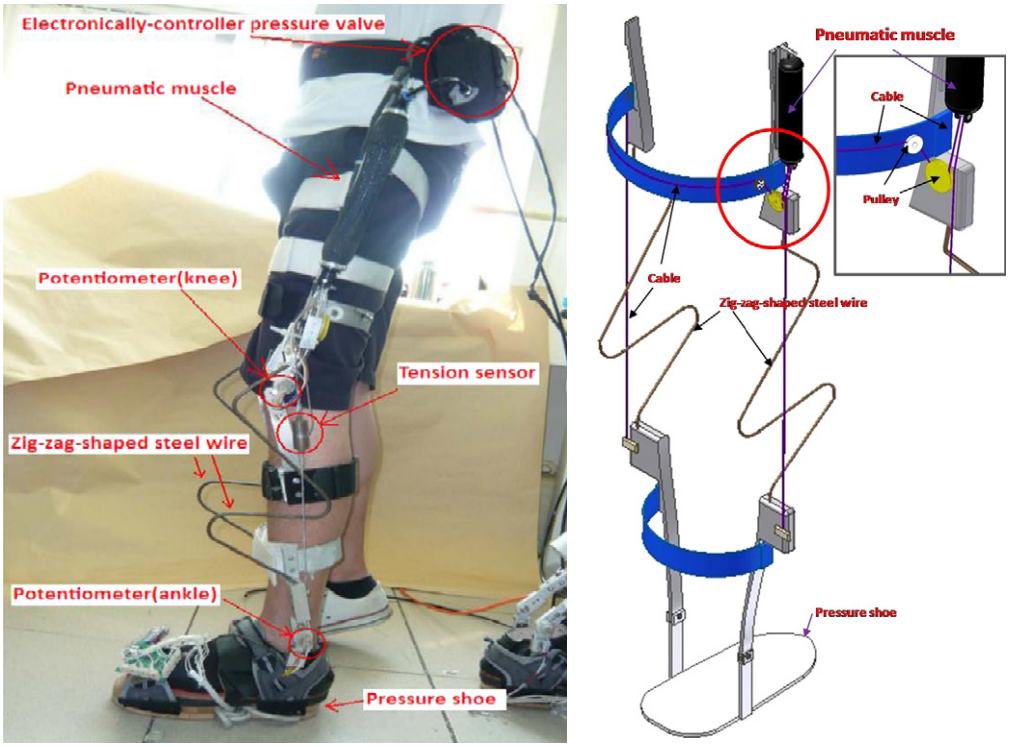

(a) Photo of the orthosis **(b) Schematic of the orthosis**

Fig. 1. Photo and schematic of the orthosis.

Fig. 2. The picture of a person wearing the orthosis system.

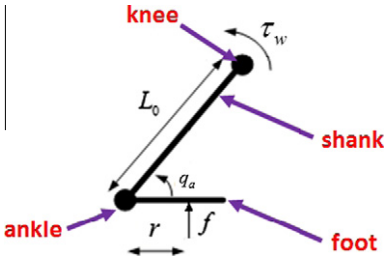

Fig. 3. The simplified shank–foot model.

these assumptions, static moment equilibrium at the knee joint gives:

$$\tau_w = f \cdot (L_0 \cos q_a - r) \tag{1}$$

where f is the ground reaction force, r is the distance from the ankle joint to the COP, q_a is the ankle angle, L_0 is the length of the shank. Denoting the assistive ratio by η, the assistive knee torque τ_a therefore is given by

$$\tau_a = \eta \cdot \tau_w = \eta \cdot f \cdot (L_0 \cos q_a - r) \tag{2}$$

It should be noted that in the literature, there are powered orthoses using the EMG signal(s) of relevant muscle(s) to directly estimate the muscle torque, consequently the assistive torque [5,6,22]. However, the EMG signal is noisy and is liable to interferences such as the skin conductance change and slight change in the positioning of electrodes [23]. It also does not give a reliable estimate of muscle force when muscle fatigue occurs [24]. Therefore, similar to the approach in [25], the measurements from the pressure shoes (f,r) and the potentiometer at the ankle (q_a) are used to estimate the muscle torque.

3. Characterization and compensation of hysteresis in pneumatic muscles

In the proposed orthosis, the pneumatic muscle converts the pneumatic energy into mechanical work by transferring the pressure applied on the inner tube into the shortening tension. The tension force generates a mechanical torque that part of this torque balances the recovering torque of the zig-zag spring and the rest of it delivers the assistive torque. Mathematically, performing torque balance on the model in Fig. 4 yields

$$\tau_a = \kappa \cdot (\theta_0 - \theta) - T \cdot L_b \cos\frac{\theta}{2} \tag{3}$$

where κ and θ_0 are respectively the torsional spring constant and the relaxed angle of the zig-zag wire, θ is the angle of the orthosis, T is the tension generated by the pneumatic muscle, and finally L_b is the length from the center of the rotation of the zig-zag wire to either end of the wire. Notice that according to Fig. 4, θ is related to L, the length of the pneumatic muscle, by the following relation:

$$\theta = 2\sin^{-1}\left(\frac{(L+L_a)}{2L_b}\right) \quad \text{or} \quad L = 2L_b \sin\left(\frac{\theta}{2}\right) - L_a \tag{4}$$

in which L_a denotes the total length between the two ends of the zig-zag steel wire.

From (3), we have $T = \frac{\kappa\cdot(\theta-\theta_0)-\tau_a}{L_b\cos\frac{\theta}{2}}$. Therefore, to achieve a desired assistive torque in the stance phase, one has to control the tension in the pneumatic muscle according to θ, consequently L by (4). Theoretically, it can be derived using the principle of the virtual work that the tension (T) and length (L) of the pneumatic muscle are related to the pressure (P) as [10]

$$T = \frac{\pi b^2}{4\pi n^2}\left(3\frac{L^2}{b^2} - 1\right)P \tag{5}$$

where b is the angle between a braided thread and the muscle's longitudinal axis, n is the number of turns of a thread. Eq. (5) represents an ideal, static model for the pneumatic muscle. It excludes the thread-on-thread Coulomb friction acting inside the braided shell. Besides, it does not consider the thickness of the inner tube and assumes that the muscle is continuously cylindrical thus ignoring the conic shape at the ends. To consider these non-ideal effects, the authors in [9,10] have also developed more sophisticated models to describe the static behavior of the pneumatic muscle. Experimentally it is found that, when the hysteresis effect is ignored, the tension force developed by the pneumatic muscle varies almost linearly with contraction ratio according to a slope globally proportional to control pressure [9]. Therefore, in [10], the constitutive relation for the pneumatic muscle is simplified as

$$\frac{T}{\Delta L} = \alpha P \tag{6}$$

where α is a constant and $\Delta L = L - L_{\min}$ with $L_{\min}$ being the minimum length of the pneumatic muscle. Because $\frac{T}{\Delta L}$ is equivalent to mechanical stiffness, such a relationship indicates that the pneumatic muscle behaves like an elastic element or a "gas spring" and the stiffness or the "spring constant" varies linearly with applied pressure.

To compare the behavior of the pneumatic muscle in the orthosis with the simplified model in (6) and to examine the impact of hysteresis effect due to Coulomb friction, a slowly-varying periodical pressure input is applied to inflate and deflate the pneumatic muscle. During the experiment, the orthosis is not worn that it is under "no-load" condition. In this case, the tension and length of the pneumatic muscle should obey (3) with $\tau_a = 0$. Fig. 5 shows how $\frac{T}{\Delta L}$, the stiffness of the pneumatic muscle, varies with the pressure P. Apparently, the stiffness is not a simple linear function of P but exhibits strong hysteresis effect so that the change of the stiffness follows two different routes for inflation ($\dot{P} > 0$) and deflation ($\dot{P} < 0$). Nevertheless, if at the given pressure, the two stiffnesses corresponding to $\dot{P} > 0$ and $\dot{P} < 0$ are averaged, it can be shown by the dash curve in Fig. 5 that the average stiffness indeed is nearly linearly proportional to the pressure. This verifies the argument that (6) can approximately portray the behavior of the pneumatic muscle if hysteresis is ignored.

In the orthosis developed, the assistive knee torque is obtained by controlling the tension in the pneumatic muscle via modulating the pressure. Although subsequently the control of the tension will be dealt with by a feedback controller, the substantial hysteresis effect observed in Fig. 5, if is not properly accounted for, may significantly deteriorate the control performance. In the following, a model which describes the hysteresis behavior is proposed and

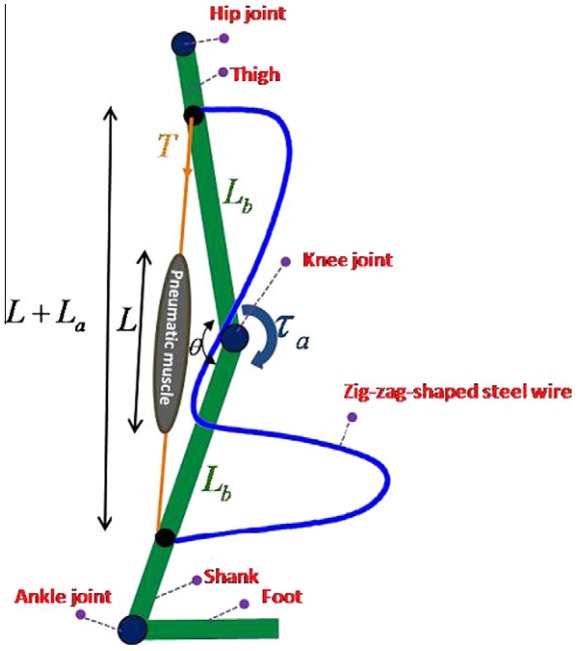

Fig. 4. The model of the orthosis.

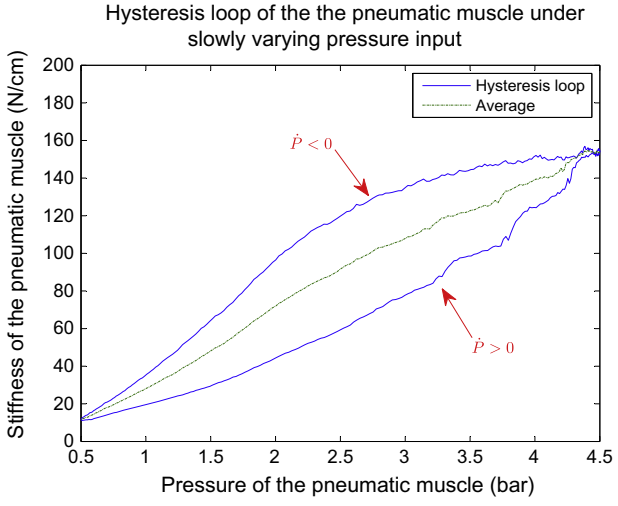

Fig. 5. A hysteresis loop of the pneumatic muscle.

the inverse of the model will be incorporated into the control system to eliminate the influence of hysteresis.

3.1. Modified maxwell-slip model for characterizing the hysteresis behavior

Due to the complex physics behind the hysteresis of the pneumatic muscle, a physics-based model is not sought here. In stead, a model which can mathematically explains the hysteretic relation between $\frac{T}{\Delta L}$ and P is developed. Such a model, although can be put in mathematical equations, can be best understood using a combination of physical elements shown in Fig. 6. In this figure, the input is the force F and the output is the associated displacement x. The force is applied to a parallel connection of a nonlinear spring with a constitutive relation $g(x)$ and a set of so-called "maxwell-slip" elements [26,27]. Each of the maxwell-slip elements is a series connection of a linear spring with a spring constant k_i, and a massless cart whose motion is subject to Coulomb friction with breakaway static friction equal to f_i ($i = 1,2,\ldots,N$). Such a model has been successfully used in [28,29] to characterize the hysteresis behavior of piezoelectric actuators. Particularly the authors therein introduced specifically the nonlinear spring element so that the overall model can generate non-anti-symmetric hysteresis loops. Due to the incorporation of the nonlinear spring, the model was referred to as the modified maxwell-slip model, as opposed to the original maxwell-slip model in [26,27] whose springs are all linear.

According to [28], the parameters k_i's, f_i's, and the function $g(\cdot)$ in the modified maxwell-slip model can be obtained via an experimental identification procedure. The procedure is outlined as follows:

- Apply a slowly-varying, positive sinusoidal input $F(t) = \frac{F_0}{2} - \frac{F_0}{2}\cos\frac{2\pi}{T_0}t$ in which F_0 denotes the size of the input and T_0 is the period. Record the $F - x$ hysteresis curve.
- On the hysteresis curve recorded, divide the interval between the maximum and minimum displacements into N equally-spaced segments. Identify as in [28] the break displacement x_i and the corresponding lower and upper break forces F_i, F_i' with $i = 0,1,2,\ldots,N$. Let the length of the equally-spaced segments be 2δ and the maxwell-slip element should follow the relation $\frac{f_i}{k_i} = i\delta$, $i = 1,2,\ldots,N$.
- Denote $g(x_i)$ by g_i with $i = 0,1,2,\ldots,N$. Identify $k_1,\ldots,k_N$, $g_0,g_1,\ldots,g_N$ by solving the constrained-minimization problem

$$\underset{k_1,\ldots,k_N,g_0,g_1,\ldots,g_N}{Min} \sum_{i=1}^{N-1}[|F_i - \widehat{F}_i(k_1,\ldots,k_N,g_0,g_1,\ldots,g_N)| + |F_i - \widehat{F}_i(k_1,\ldots,k_N,g_0,g_1,\ldots,g_N)|] \quad (7)$$

subject to

(i) $k_1,\ldots,k_N > 0$

(ii) $$\widehat{F}_i = F_0 - 2\delta\sum_{m=1}^{i} m\cdot k_m - 2i\cdot\delta\sum_{m=i+1}^{N} k_m + g_i - g_0 \quad (8)$$

$$\widehat{F}_i' = 2\delta\sum_{m=1}^{i} m\cdot k_m + 2i\cdot\delta\sum_{m=i+1}^{N} k_m + g_{N-i} - g_N \quad (9)$$

It should be noted that according to the derivation in [28], $\widehat{F}_i\left(\widehat{F}_i'\right)$ in the second constraint corresponds to the breaking force that the ith massless cart is just about to slide when $\dot{F} > 0$ ($\dot{F} < 0$). Moreover, the first constraint, composed by linear inequalities in k_i's, assures that the linear springs in the model are always positive. Because the cost function is in $1-norm$ structure and the constraints are linear functions of k_i's, and g_i's, the optimization problem can be solved by linear programming. Finally, once all the parameters are identified, the model can be directly inversed [28,29]. In the inverse model, using the input x together with the sign of $\dot{x}$, one can compute the forces generated by the nonlinear spring, the linear spring and the maxwell-slip elements. Summing up these forces provides the output F.

3.2. Characterization and compensation of hysteresis using the modified maxwell-slip model

The hysteresis in the pneumatic muscle is caused by the thread-on-thread friction which is proportional to thread-on-thread pressure. Assuming that the pressure inside the inner tube transmits entirely to the shell, the thread-on-thread pressure is equal to the inflation muscle pressure P [9]. Consequently, P is the main cause of Coulomb friction thus the hysteresis. When the modified maxwell-slip model is used to mathematically model the hysteresis in pneumatic muscles, the pressure P should replace F as the input. On the other hand, because P and $\frac{T}{\Delta L}$ follow the linear relation in (6) when hysteresis and nonlinearity are ignored, the stiffness $\frac{T}{\Delta L}$ will take the place of displacement x in the model.

The experimental identification procedure mentioned is used to obtain the parameters of the hysteresis model. Under the "no-load" condition, the pneumatic muscle is excited by 0.1 Hz positive

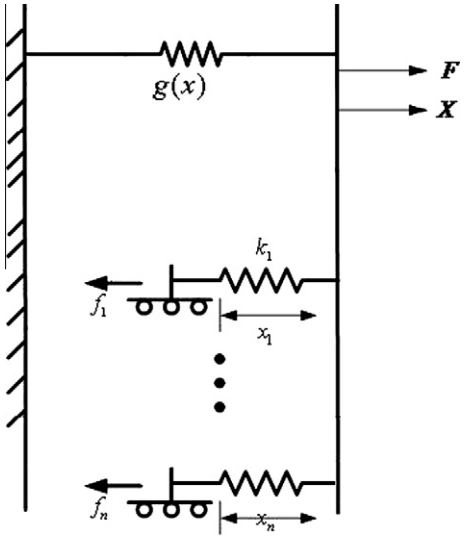

Fig. 6. The modified maxwell-slip model.

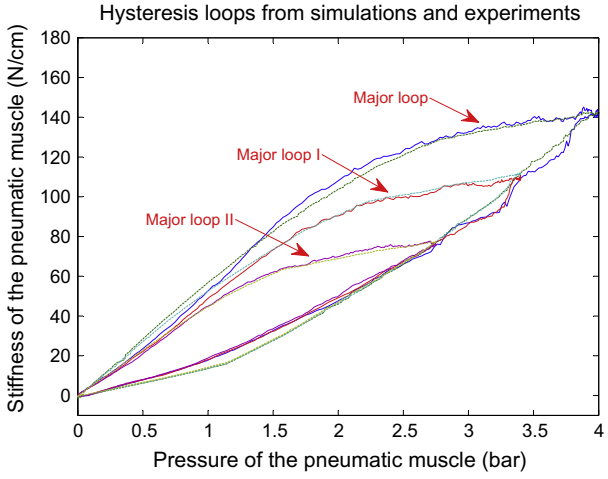

Fig. 7. The hysteresis loops from simulation and experiment.

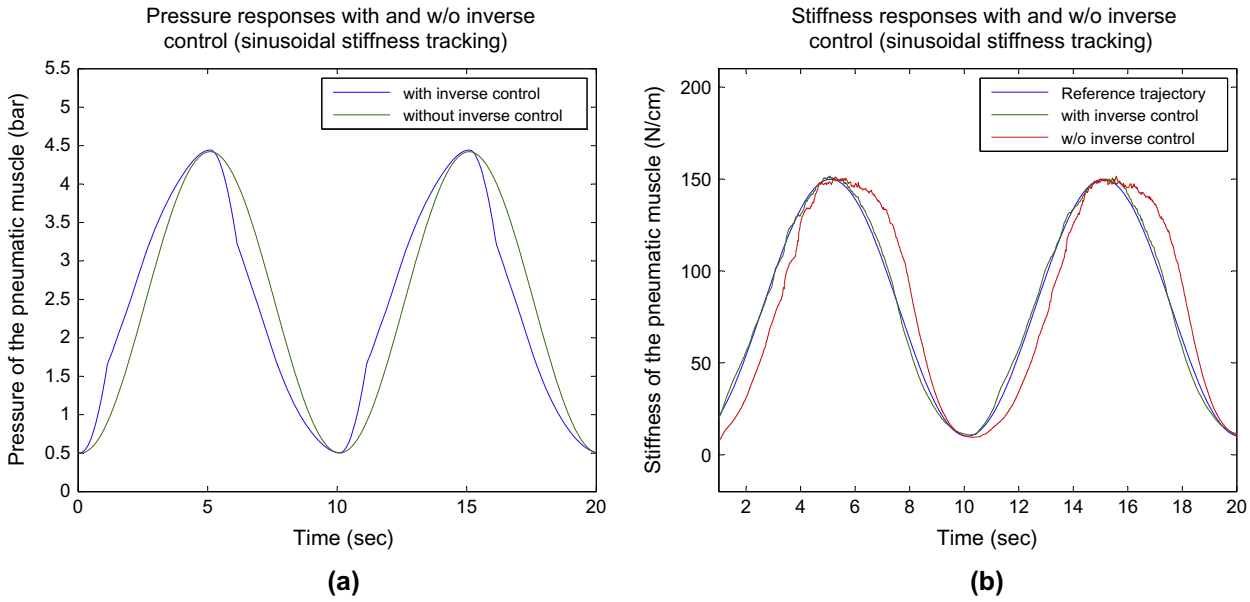

Fig. 8. Pressure and stiffness responses of sinusoidal stiffness tracking with and w/o inverse control.

sinusoidal pressure profiles of three different peak amplitudes to generate one major and two minor hysteresis loops shown in the experimental curves of Fig. 7. While the data from the major and the small minor loops are used in the optimization problem to solve for the model parameters, the data from the medium minor loop is used for model validation. Notice that the adoption of P and $\frac{T}{\Delta L}$ respectively as the input and output makes the modified maxwell-slip model lose its physical meaning, so k_i's, and f_i's (or g_i's) no longer represent spring constants and forces. In stead, the units should be changed to cm^{-1} for k_i's, and to $\mathrm{N\,cm}^{-2}$ for f_i's and g_i's. In Fig. 7, the input–output response of the identified model is simulated and is found to closely match experimental curve. For the major loop, the maximum error is about 5.7% of the stiffness range. For the medium and the small loops, the maximum errors are about 6% and 7.7% respectively.

The identified model is used to devise to an inverse control law to cancel the hysteresis nonlinearity. An experiment is performed under the "no-load" condition to verify the performance of the inverse control. In the inverse control experiment, the identified model is inversed to compute the input pressure profile corresponding to a sinusoidal stiffness trajectory with frequency of 0.1 Hz and an amplitude of $70\ \mathrm{N\,cm}^{-1}$. Fig. 8a shows the pressure computed by the inverse control law as well as the sinusoidal pressure profile computed based on the nominal pressure–stiffness ratio. In Fig. 8b the stiffness responses corresponding to the two cases are compared. The RMS tracking error achieved by the inverse control is about 2.07%, as opposed to 11.11% in the sinusoidal input case.

4. Control system design

As mentioned previously, in the proposed orthosis, tension control is needed for the stance phase and trajectory control is needed for the swing phase. The inverse control for hysteresis compensation, which can be viewed as a feedforward action and thus is sensitive to disturbances and unmodelled dynamics, cannot achieve the control performance alone in either cases. Therefore, in this section, two feedback controllers are designed to respectively regulate the tension of the pneumatic muscle and the angle of the orthosis. The inverse control introduced will then be incorporated into the control systems to further enhance the performance. Finally, bumpless switching of the control action between the two phases will be discussed.

4.1. Frequency response and LTR control

To design the feedback controllers, frequency response tests are performed experimentally to identify the linearized dynamics of the orthosis. During the tests, the orthosis is under "no-load" condition and the pneumatic muscle is first inflated to an operating condition with nominal pressure, nominal length, and nominal tension equal to 2 bar, 22 cm, 158 N. The pressure (P) is then perturbed sinusoidally with frequency ranging from to 0.1 Hz to 2 Hz, and the resultant responses in tension (T) of the pneumatic muscle and the angle of the orthosis (θ) are measured. The two experimental frequency responses from the perturbed pressure δP to the perturbed tension δT, and from δP to the perturbed orthosis angle $\delta\theta$ are respectively measured. Using the frequency responses, the nominal transfer functions $G_T(s) = \frac{\delta T(s)}{\delta P(s)}$, and $G_\theta(s) = \frac{\delta\theta(s)}{\delta P(s)}$ associated with the linearized dynamics can be numerically identified. Take $G_T(s)$ for instance, it is given by

$$G_T(s) = \frac{572.157(s^2+17.45s+75.79)(s^2+7.39s+13.41)}{(s+12.33)(s^2+17.97s+78.51)(s^2+13.78s+47.43)(s^2+8.11s+17.12)} \quad (10)$$

Once the nominal transfer functions are obtained, loop-transfer-recovery (LTR) control methodology [30] is used to design the controllers $K_T(s)$ and $K_\theta(s)$ for respectively achieving tension control and angle control. The design procedure of LTR methodology automatically guarantees that the closed-loop stability with respect to the nominal transfer function. Notice that when designing either one of controllers, in order for it to be stiff to reject disturbances at low frequencies, an integrator is firstly augmented to the nominal transfer function ($G_T(s)$ or $G_\theta(s)$) and then the LTR design is conducted on the state-space representation of the augmented plant. LTR is a linear quadratic Gaussian (LQG) optimal control based method. The design procedure requires one to solve two algebraic Riccati equations: one corresponds to the Linear Quadratic Regulator problem, and the other to the Kalman filter problem. As shown in [30], by implementing the cheap control

LQR problem in LQG, the system loop transfer function can be recovered to a Kalman filter loop transfer function which mimics a pure integrator with a bandwidth equal to $\frac{1}{\sqrt{\mu}}$, where μ is a fictitious output noise intensity. This indicates that the LTR design allows one to designate the closed-loop system bandwidth by the choice of μ. Again taking the tension control for example, the controller $K_T(s)$ is given by

$$K_T(s)=\frac{\begin{array}{l}6.418\times10^4s^7+6.679\times10^6s^6+2.892\times10^8s^5+6.714\times10^9s^4+8.96\times10^{10}s^3\\+6.816\times10^{11}s^2+2.713\times10^{12}s+4.343\times10^{12}\end{array}}{\begin{array}{l}s^9+215.7s^8+2.038\times10^4s^7+1.138\times10^6s^6+4.213\times10^7s^5\\+1.054\times10^9s^4+1.623\times10^{10}s^3+1.304\times10^{11}s^2+3.948\times10^{11}s\end{array}} \tag{11}$$

The achieved closed-loop bandwidth is 26.2 Hz for $K_T(s)$ (and is 14.4 Hz for $K_\theta(s)$). The bandwidths are chosen so that they are sufficiently high for performance sake and still the control systems are robustly stable against the error between the experimental frequency response and the nominal transfer functions $G_T(s)$ or $G_\theta(s)$.

The inverse control developed previously is integrated with either $K_T(s)$ or $K_\theta(s)$ to compensate for hysteresis so that the linearization-based controller can work more effectively. The tension control system and the angle trajectory control systems are shown respectively in Fig. 9a and b. Notice that in Fig. 9a, the desired tension force T_d equals $\frac{\kappa\cdot(\theta-\theta_0)-\tau_a}{L_b\cos\frac{\theta}{2}}$ in which the assistive torque τ_a is computed using (2) and the measurements from the pressure shoe and the ankle sensor. The inverse control algorithm in this case firstly divides the desired tension force T_d by the measured length ΔL in real time to obtain the desired stiffness. Then it computes a feedforward pressure which leads to the desired stiffness, consequently the desired tension T_d. The controller $K_T(s)$ further reduces the force tracking error via feedback. On the other hand, the desired angle trajectory θ_d in Fig. 9b is obtained from measuring the knee motion of a person during normal swinging. The inverse control algorithm provides a feedforward pressure which leads to a desired tension force that can counteract the recovering torque of the zig-zag wire. The desired tensor force in this case is computed as $\frac{\kappa\cdot(\theta-\theta_0)}{L_b\cos\frac{\theta}{2}}$ by setting $\tau_a=0$ in (3). After the recovering torque is compensated, the feedback controller $K_\theta(s)$ further fine-tunes the pressure to achieve the tracking performance.

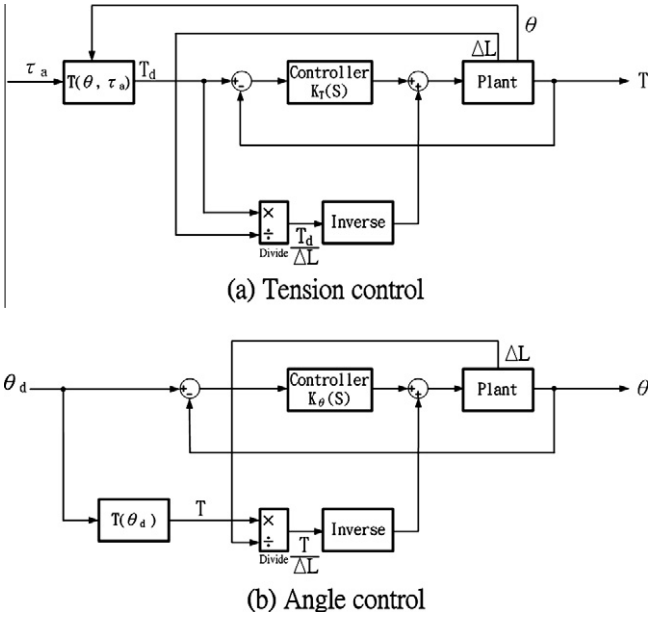

Fig. 9. Block diagrams for tension control and angle control.

4.2. Bumpless switching between $K_T(s)$ and $K_\theta(s)$

For the proposed orthosis, the switch between stance phase and swing phase, consequently between $K_T(s)$ and $K_\theta(s)$ is activated by the three loadcells located near the heel of the pressure shoe. When the average weight measured by these loadcells are higher than a threshold (=5 kg), the operation is classified as the stance phase; otherwise, it is classified as the swing phase. During walking or climbing stairs, the orthosis has to periodically switch between the two phases. In order to assure the control action is transferred smoothly between $K_T(s)$ and $K_\theta(s)$, two bumpless switching compensators similar to the one proposed in [31] are used. The block diagram of the combined control system is shown in Fig. 10. In this figure, while compensator I provides smooth switching when $K_T(s)$ takes over the control action, compensator II assures the control continuity when switching into the swing phase. For graphical clarity, the inverse controllers are not shown in Fig. 10, but they are still employed to cancel hysteresis.

To provide bumpless switching, both compensators (I and II) and controllers ($K_T(s)$ and $K_\theta(s)$) are turned on all the time except that during the stance phase the output of $K_T(s)$ determines the pressure of the pneumatic muscle and during the swing phase, the pressure is determined by the output of $K_\theta(s)$ instead. The design of compensator I(II) is based on the state-space realization of $G_T(s)$ ($G_\theta(s)$). Take compensator I for example. Assume that the state equations of $G_T(s)$ is given by

$$\begin{aligned}\dot{\mathbf{x}}&=\mathbf{A}\mathbf{x}+\mathbf{B}u\\ y&=\mathbf{C}\mathbf{x}\end{aligned} \tag{12}$$

where $\mathbf{x}$ is the state, u is the plant input (which corresponds to δP), y is the output (which corresponds to δT), and $\mathbf{A}$, $\mathbf{B}$, $\mathbf{C}$ are the matrices of suitable dimensions. Then compensator I has the following state-space form:

$$\begin{aligned}\dot{\xi}&=\mathbf{A}\xi+\mathbf{B}(u-u_T)\\ v_{T_1}&=\mathbf{K}\xi+L(u-u_T)\\ v_{T_2}&=\mathbf{C}\xi\end{aligned} \tag{13}$$

In this form, ξ is the compensator's state, and v_{T_1}, v_{T_2} are the outputs, u_T is the output of the controller $K_T(s)$. $\mathbf{K}$, L are respectively a matrix and a parameter obtained by solving a set of linear matrix inequalities (LMI's) to guarantee the stability of compensation [31]. During the swing phase, u is the output of $K_\theta(s)$. Although the output of $K_T(s)$ is not connected to the orthosis, the controller still uses the measured tension and desired tension $\frac{\kappa\cdot(\theta-\theta_0)-\tau_a}{L_b\cos\frac{\theta}{2}}$ with $\tau_a=0$ to perform control computation. The existence of compensator I ensures that u_T, the output $K_T(s)$ does not diverge, and when switching to the stance phase, the control

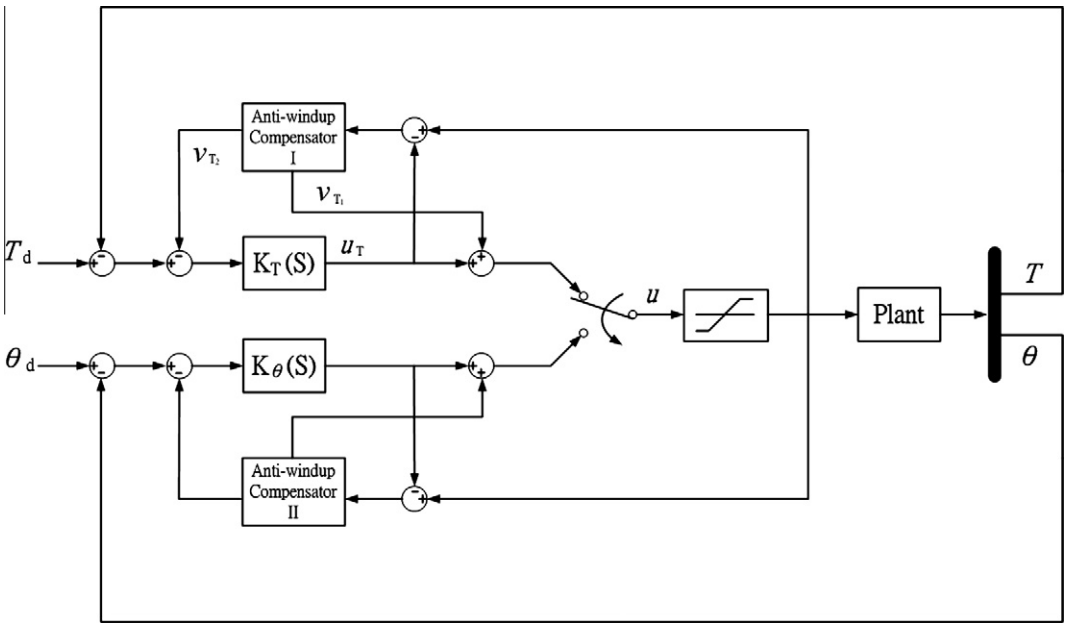

Fig. 10. Closed-loop control with bumpless switching.

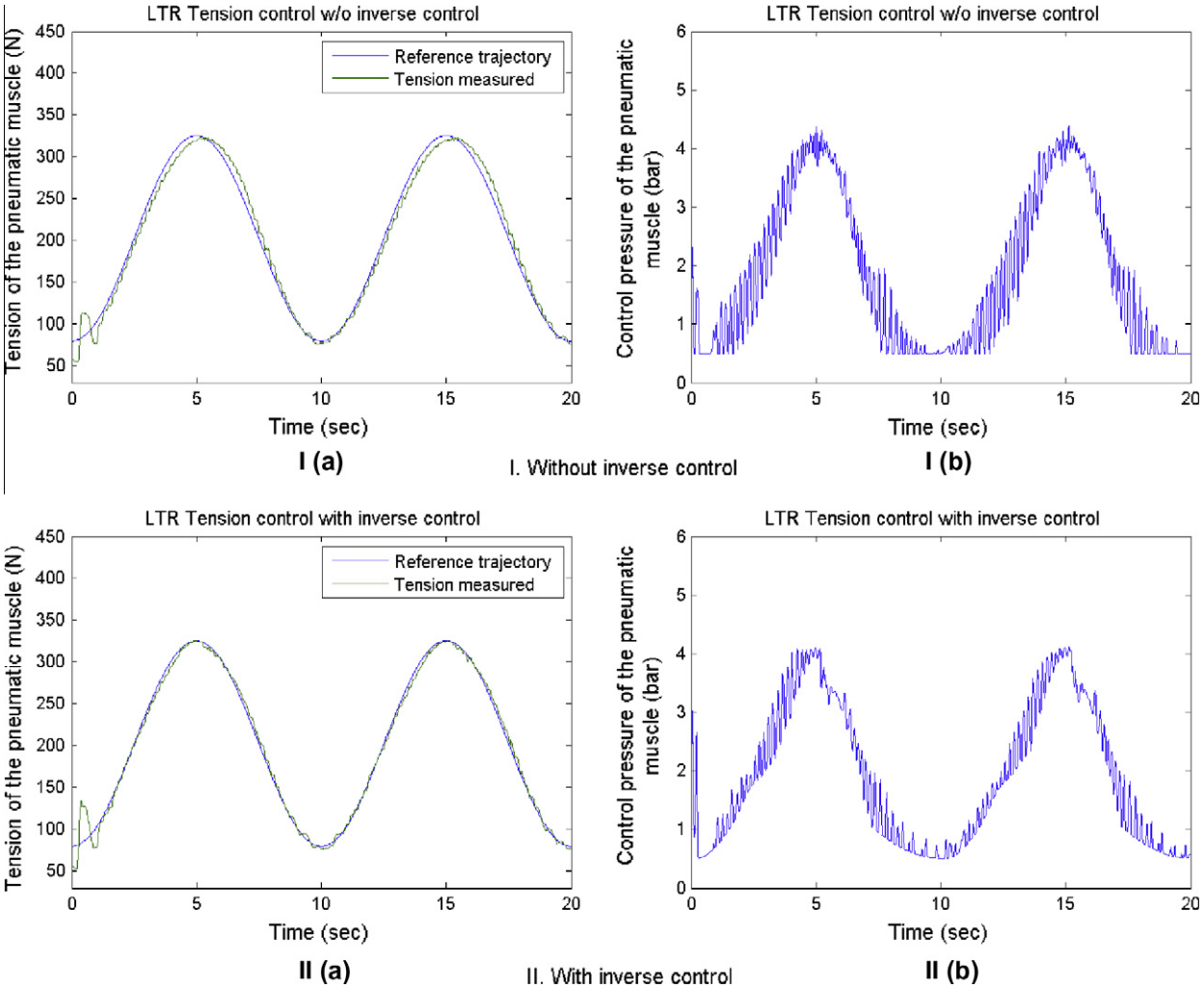

Fig. 11. Tension and pressure responses for LTR tension tracking.

transience can die out quickly. The design and operation of compensator II is similar to those of compensator I except that the desired angle trajectory θ_d during the stance phase is set to the actual knee angle θ.

Finally according to [31], the compensators designed not only perform bumpless switchings but also can be used to avoid integrator windup caused by control saturation. Therefore, in Fig. 10, a saturation block is also inserted so that the signal u is the saturated input to the plant. For the proposed orthosis, take compensator I for example, $\mathbf{K} = [-\mathbf{4.7554} \times \mathbf{10^{-6}}, \ -\mathbf{1.8426} \times \mathbf{10^{-4}}, \ -\mathbf{0.0028}, -\mathbf{0.0221}, \ -\mathbf{0.0977}, \ -\mathbf{0.2285}, \ -\mathbf{0.2198}]$, $\mathbf{L} = -1.4758$. The stability proof of the bumpless switching compensation can be found in [31].

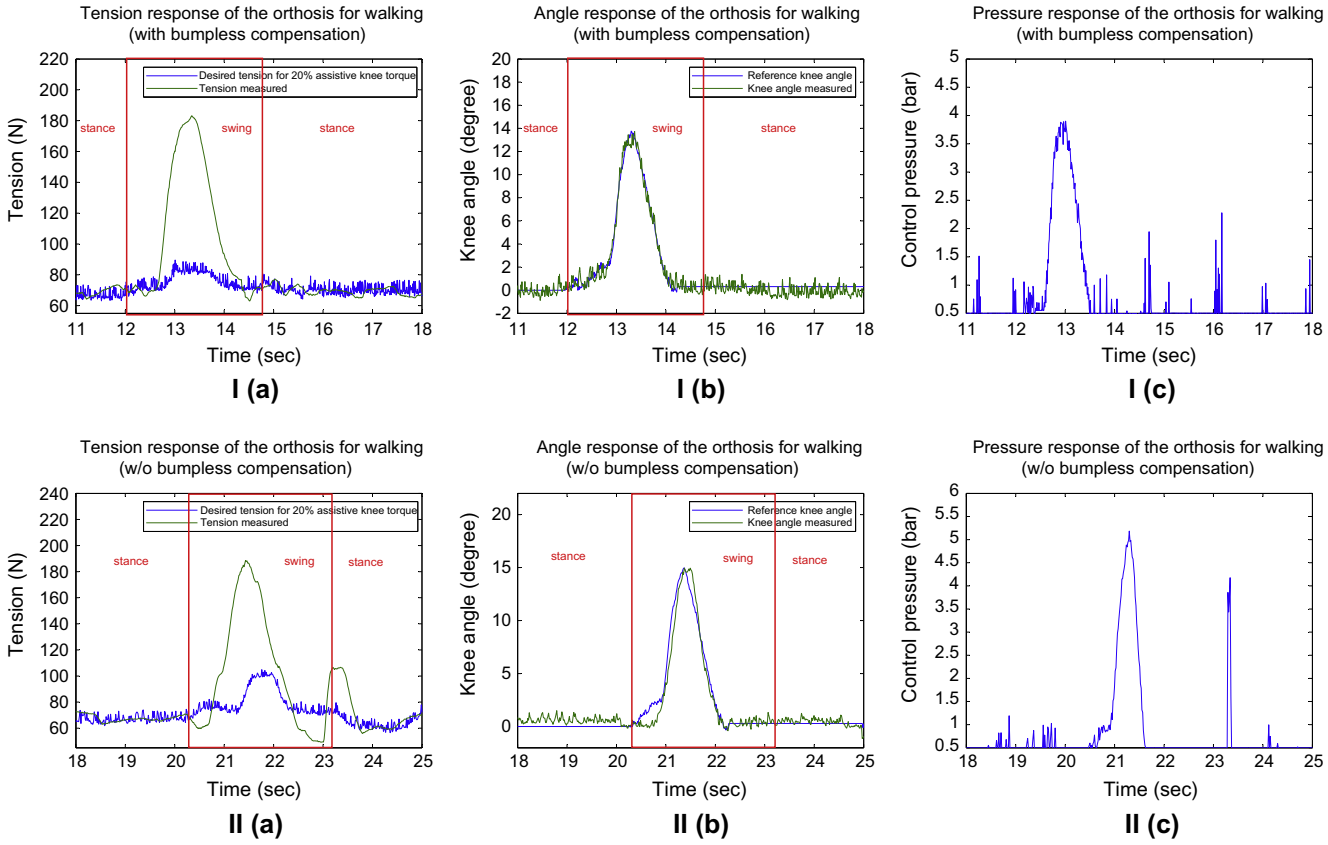

Fig. 12. Tension, angle, and pressure responses of the orthosis for walking with bumpless compensation and w/o bumpless compensation.

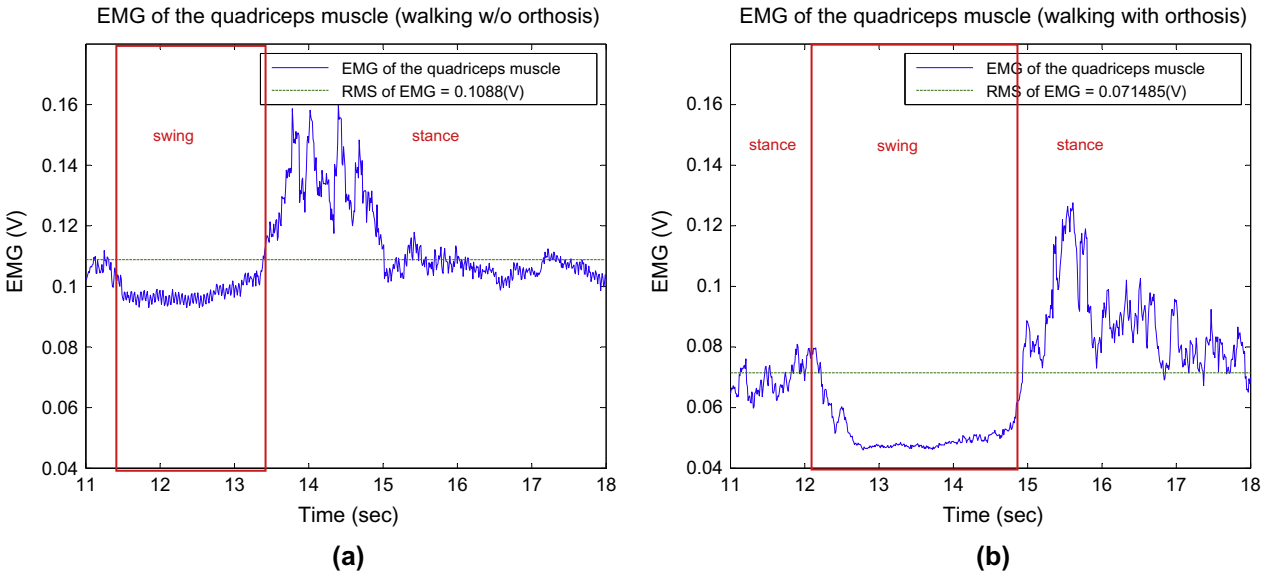

Fig. 13. Comparison of EMG signals with and w/o orthosis (walking).

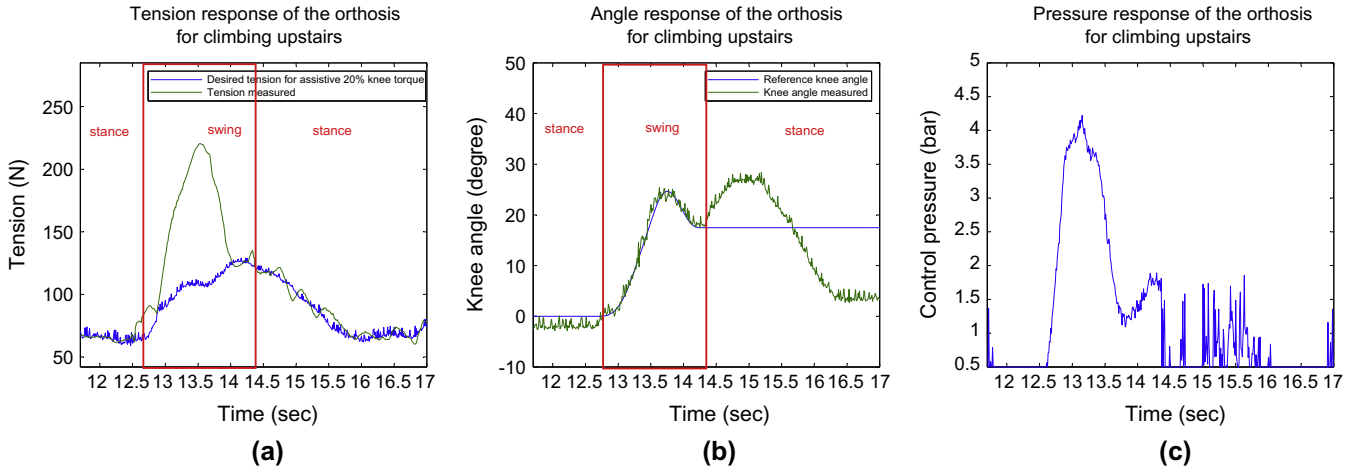

Fig. 14. Tension, angle, and pressure responses of the orthosis for climbing upstairs.

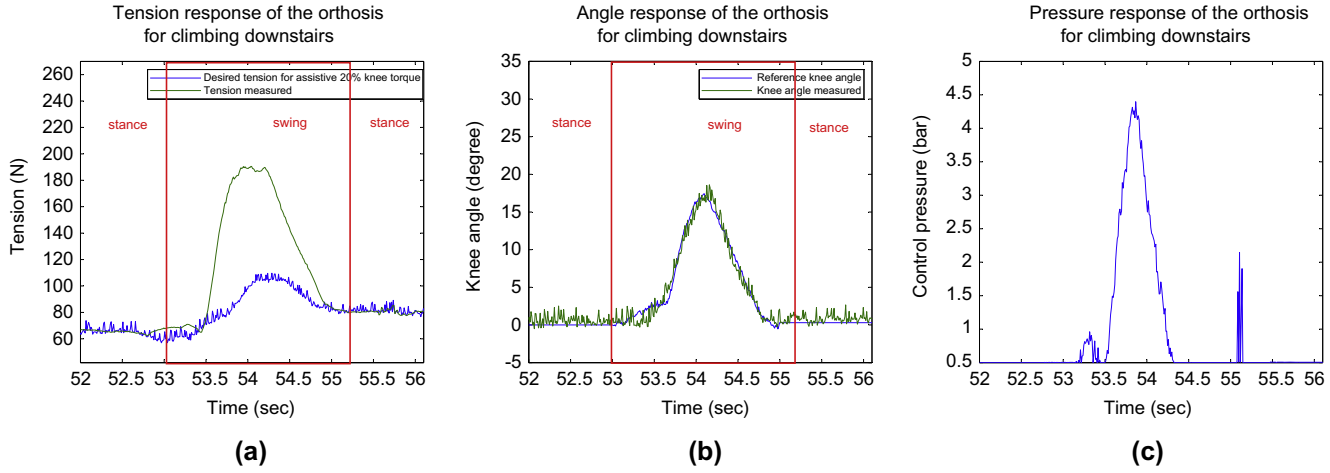

Fig. 15. Tension, angle, and pressure responses of the orthosis for climbing downstairs.

5. Experiments and performance evaluation

In this section, several experiments are conducted to examine the performance of the control system designed for the powered orthosis.

5.1. Tension tracking under "no-load" operation

To illustrate the usefulness of incorporating the inverse control into the LTR control system, tension tracking under "no-load" operation is performed. The control system is demanded to track a sinusoidal tension with frequency of 0.1 Hz and an amplitude of 125 N. During the experiment, firstly only the feedback controller $K_T(s)$ is used and the tension response and pressure response are measured and shown respectively in Fig. 11Ia and Ib. Because the hysteresis effect is not compensated for, the tension response lags behind the reference trajectory noticeably. Next the control system in Fig. 9a is used. The tension response and pressure response are shown respectively in Fig. 11IIa and IIb. Apparently, with the incorporation of inverse control, the tracking performance is greatly improved. It should be noted that at the beginning of the control process, the initial tension of the pneumatic muscle (≈55 N) is significantly different from the reference tension setting (≈80 N), so there are some oscillations during the control transience. After about 2 s, the control transience dies out and accurate tension tracking is achieved. The RMS tracking error in this case is reduced to within 1.33%. Such a track performance is also about 3.5 times better than that in Fig. 11Ia in which the inverse control is not used.

5.2. Walking experiments

In the walking experiments, a human subject wears the orthosis and performs regular walking. The combined control system in Fig. 10 is used to deal with the stance phase, the swing phase and the transition between the two phases. In the experiment, considering the maximum pressure capacity of the pneumatic muscle (≈4.5 bar), the assistive ratio is set to 20%.[3] Because the noises contained in the load cells, the desired assistive torque computed using (2) is filtered by an eighth-order Butterworth low-pass filter with a passband edge frequency of 5 Hz before it is injected to the control system as the reference signal. The reference angle trajectory $\theta_d(t)$ for the swing phase is obtained from measuring a normal person's knee joint trajectory during walking.

[3] It is shown in the subsequent experimental pressure responses that with 20% assistive ratio, the peak of the pneumatic muscle's pressure nearly reaches its maximum capacity. Therefore, for safety reason as well as avoiding the control performance degradation due to pressure saturation, the maximum assistive ratio is set to 20% in the current investigation.

The tension, angle, and the pressure responses of the orthosis during one walking cycle are shown respectively in Fig. 12Ia–Ic. From Fig. 12Ia and Ib, one can see that the control system can provide quite satisfactory tension tracking (during the stance phase) and angle tracking (during the swing phase). Moreover, the responses in tension, angle both exhibit quite smooth behaviors when phase transition occurs. For verifying that the smooth behavior is contributed by the bumpless compensators, the bumpless compensators are deliberately turned off and the relevant responses are measured and shown in Fig. 12IIa–IIc. Clearly, without the compensators, the responses exhibit quite oscillating behavior right after phase transition. According to the operator, the transience induced by control switching also causes discomfort to the lower limb.

Finally, in order to verify that the proposed orthosis indeed provides assistive function, the EMG signals of the quadriceps muscle before and after the orthosis is worn are measured and shown in Fig. 13a and b. During the experiments, the data associated with five strides were taken but for clarity only the data within one stride are shown in Fig. 13. Before the orthosis is worn, the RMS magnitude of the EMG signal for the five strides performed is 0.11 V. With the help of the orthosis, the RMS magnitude is reduced to 0.07 V. This verifies the usefulness of the orthosis in assisting human walking.

Notice that in the current experiments, the operator walks gently at the pace of 5 s per stride. If the operator walks faster, then the dynamic effect becomes prominent and (2) no longer provides a good estimate for the assistive torque. In this case, the orthosis may assist the knee motion in a faulty manner which would cause discomfort to the operator. Furthermore, the dynamic effect would certainly demand higher peak pressure from the pneumatic muscle. Therefore, for safety and performance reasons, walking in a faster pace is not considered in the current investigation.

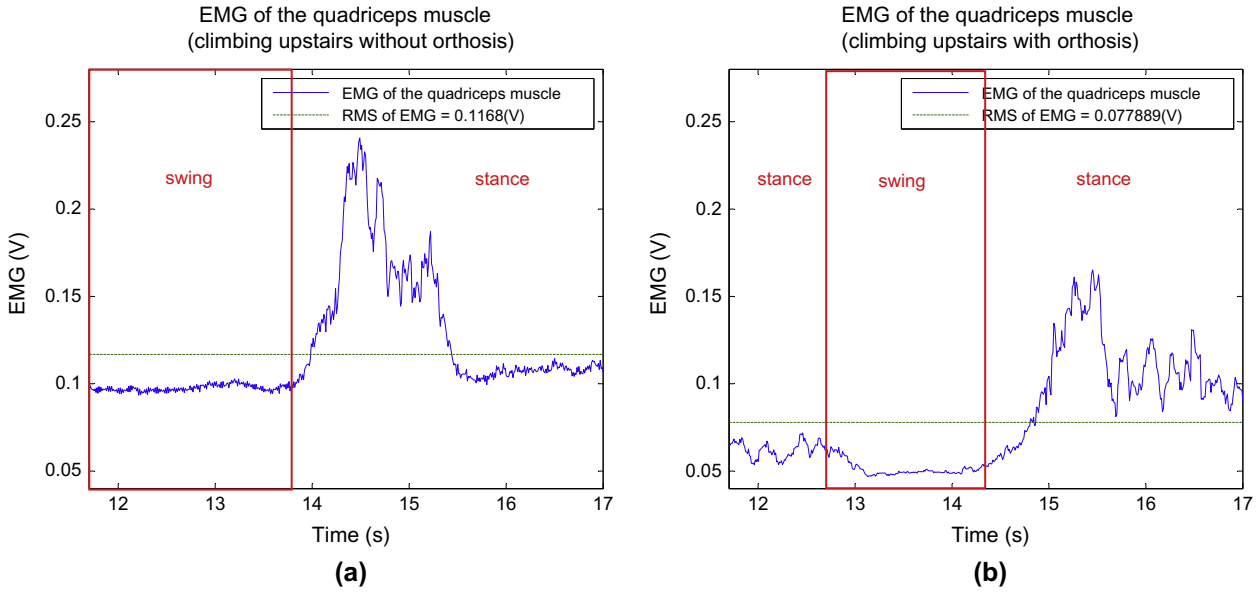

Fig. 16. Comparison of EMG signals with and w/o orthosis (climbing upstairs).

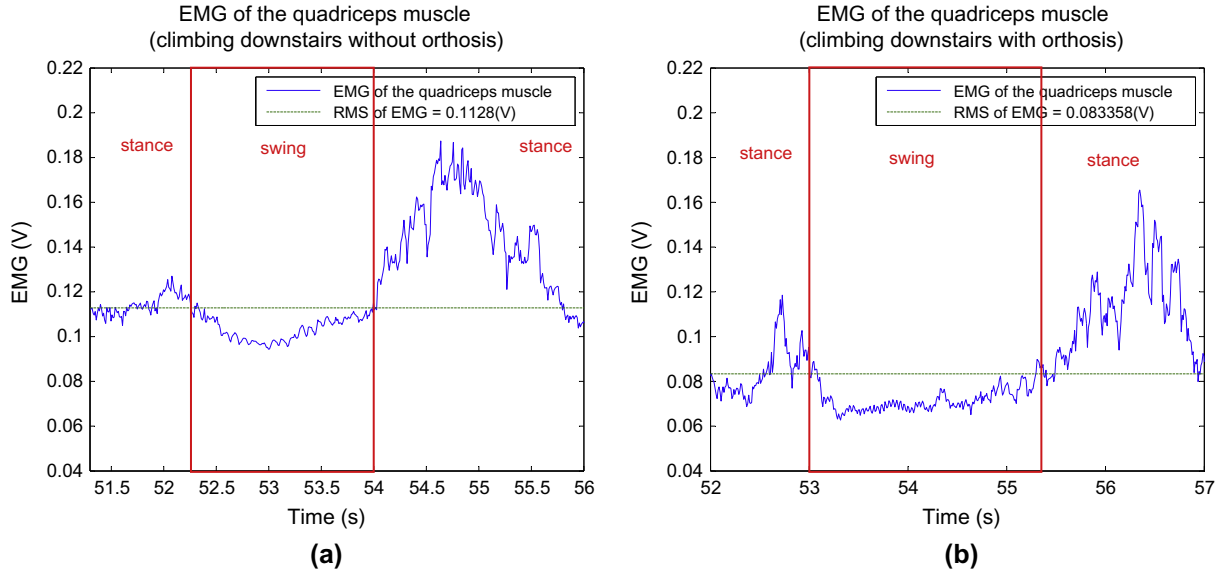

Fig. 17. Comparison of EMG signals with and w/o orthosis (climbing downstairs).

5.3. Stair climbing experiment

In the stair climbing experiments, the combined control system with bumpless transfer compensators is used. The assistive ration is still set to 20%. The stairs have a step width of 60 cm and a height of 17 cm. Figs. 14 and 15 respectively show the experimental responses for the climbing up and climbing down cases. The EMG signals of the quadriceps muscle before and after the orthosis is worn for the two cases are also shown in Figs. 16 and 17. By RMS calculation, the EMG signals after wearing the orthosis are reduced respectively by 33% and 26.1%. This indicates that the developed orthosis is also effective in assisting the stair-climbing motion.

6. Conclusions

In this paper, control of McKibben pneumatic muscles for a power-assist, lower-limb orthosis is considered. For eliminating the influence of hysteresis on the control performance, a modified maxwell-slip model is proposed to describe hysteresis and to devise an inverse control method. The inverse control is then combined with LTR feedback control to achieve better tracking performance. To ensure the control of the orthosis can switch smoothly between the stance phase and the swing phase, two bumpless switching compensators are further incorporated into the combined control system. Experiments show that the control system can make the orthosis effectively accomplish the assistive function. In the orthosis developed, the two compressed CO_2 tanks, which contribute the most of the 4 kg weight of the backpack, are not only heavy but also bulky. Moreover, during the operation the gas they supplied can only last for about 40 min. Regardless of the control performance achieved, to increase the portability of the orthosis, weight and capacity issues associated with the pneumatic sources need to be resolved. Therefore, current research efforts are devoted to seeking pneumatic sources with lighter weight and higher capacity.

Acknowledgment

The authors gratefully acknowledge the support provided by National Science Council in Taiwan.

References

[1] Gavrilovic MM, Maric MR. Positional servo-mechanism activated by artificial muscles. Med Biol Eng 1969;7:77–82.
[2] Schulte Jr HF, The characteristics of the McKibben artificial muscle. In: The application of external power in prosthetics and orthotics. Washington (DC): National Academy of Sciences – National Research Council; 1961.
[3] Kobayashi H, Hasegawa S, Nozaki H. Development of muscle suit for supporting manual worker. In: SICE annual conference, Japan; September 2007. p. 618–22.
[4] Zhang J-F et al. Modeling and control of a curved pneumatic muscle actuator for wearable elbow exoskeleton. Mechatronics 2008;18:448–57.
[5] Ferris DP, Czerniecki JM, Hannaford B. An ankle–foot orthosis powered by artificial pneumatic muscles. J Appl Biomech 2005;21(2):189–97.
[6] Sawicki GS, Ferris DP. A pneumatically powered knee–ankle–foot orthosis (KAFO) with myoelectric activation and inhibition. J Neuroeng Rehab 2009:6–23.
[7] Costa N, Caldwell DG. Control of a biomimetic soft-actuated 10 DOF lower body exoskeleton. In: The first IEEE/RAS–EMBS international conference on biomedical robotics and biomechatronics; 2006. p. 496–501.
[8] Davis S et al. Enhanced modelling and performance in braided pneumatic muscle actuators. Int J Robot Res 2003;22(3–4):213–27.
[9] Tondu B, Lopez P. Modeling and control of McKibben artificial muscle robot actuators. IEEE Contr Syst Mag 2000:15–38.
[10] Chou C-P, Hannaford B. Measurement of modeling of McKibben pneumatic artificial muscles. IEEE Trans Robot Automat 1996;12(1):90–102.
[11] Klute GK, Hannaford B. Fatigue characteristics of McKibben artificial muscle actuators. In: IEEE/RSJ international conference on intelligent robots and systems, Victoria, BC, Canada; 1998. p. 1776–82.
[12] Klute GK, Hannaford B. Accounting for elastic energy storage in McKibben artificial muscle actuators. J Dynam Syst, Measure Contr 2000;122:386–8.
[13] Reynolds DB, Repperger DW, Phillips CA, Bandry G. Modeling the dynamic characteristics of pneumatic muscle. Ann Biomed Eng 2003;31:310–7.
[14] Klute GK, Czerniecki JM, Hannaford B. McKibben artificial muscles: pneumatic actuators with biomechanical intelligence. In: IEEE/ASME international conference on advanced intelligent Mechatronics, Atlanta, GA; 1999. p. 221–6.
[15] Klute GK, Czerniecki JM, Hannaford B. Artificial muscles: actuators for biorobotic systems. Int J Robot Res 2002;21:295–309.
[16] Aschemann H, Schindele D. Sliding-mode control of a high-speed linear axis driven by pneumatic muscle actuators. IEEE Trans Ind Electron 2008;55(11):3855–64.
[17] Van-Damme M et al. Proxy-based sliding mode control of a manipulator actuated by pleated pneumatic artificial muscles. In: Proceedings of IEEE international conference on robotics and automation, Rome, Italy; 2007. p. 4355–60.
[18] Thanh TDC, Kwan AK. Intelligent control of 2 axes pneumatic artificial muscle manipulator. In: Proceedings of international symposium on electrical and electronics engineering, Vietnam; 2007. p. 14–9.
[19] Aschemann H, Hofer EP. Flatness-based trajectory planning and control of a parallel robot actuated by pneumatic muscles. In: Proceedings on ECCOMAS thematic conference multibody dynamics, Spain; 2005.
[20] Zhu X et al. Adaptive robust posture control of parallel manipulator driven by pneumatic muscles with redundancy. IEEE/ASME Trans Mechatron 2008;13(4):441–50.
[21] Shaw D, Huang C-R, Huang L-C. Design of non-linear beam-type spring for designated loading and displacement for use in lower-limb orthosis. Comput, Mater, Continua 2009;11(3):229–42.
[22] Hayashi T, Kawamoto H, Sankai Y. Control method of robot suit HAL working as operator's muscle using biological and dynamic information. IEEE/RSJ international conference on intelligent robots and systems; 2005. p. 3063– 8.
[23] Fleischer C et al. Online calibration of the EMG to force relationship. In: IEEE/RSJ international conference on intelligent robots and systems; 2004. p. 1305–10.
[24] Hyun BR et al. EMG-based neural networks for muscle torque estimation. In: 11th annual conference of the international FES society; 2006. p. 240–3.
[25] Pratt JE, Krupp BT, Morse CJ. The RoboKnee: an exoskeleton for enhancing strength and endurance during walking. In: IEEE international conference on robotics & automation; 2004. p. 2430–5.
[26] Karnopp D. Computer models of hysteresis in mechanical and magnetic components. J Franklin Inst 1983;316(5):405–15.
[27] Goldfarb M, Celanovic N. Modeling piezoelectric stack actuators for control of micromanipulation. IEEE Contr Syst Mag 1997;17:69–79.
[28] Yeh T-J, Lu Shin-Wen, Wu Ting-Ying. Modeling and identification of hysteresis in piezoelectric actuators. ASME J Dynam Syst, Measure 2006;128(2):189–96.
[29] Yeh T-J, Hung Ruo-Feng, Lu Shin-Wen. An integrated physical model that characterizes creep and hysteresis in piezoelectric actuators. Simulat Modell Practice Theory 2008;16(1):93–110.
[30] Athans M. A tutorial on the LQG/LTR method. In: Proceedings of the American control conference, Seattle, WA; June 1986.
[31] Zaccarian L, Teel AR. A common framework for anti-windup, bumpless transfer and reliable designs. Automatica 2002(38):1735–44.